

# X-ray fluorescence microtomography based on polycapillary-focused X-rays from laboratory source

Bing-Gang Feng<sup>1,2</sup> · Fen Tao<sup>1,2</sup> · Yi-Ming Yang<sup>1,2</sup> · Tao Hu<sup>1,2</sup> · Fei-Xiang Wang<sup>1,2</sup> · Guo-Hao Du<sup>1</sup> · Yan-Ling Xue<sup>1</sup> · Ya-Jun Tong<sup>1</sup> · Tian-Xi Sun<sup>3</sup> · Biao Deng<sup>1</sup> · Ti-Qiao Xiao<sup>1,2</sup>

Received: 23 May 2017 / Revised: 30 November 2017 / Accepted: 14 December 2017 / Published online: 30 April 2018  
© Shanghai Institute of Applied Physics, Chinese Academy of Sciences, Chinese Nuclear Society, Science Press China and Springer Nature Singapore Pte Ltd. 2018

**Abstract** X-ray fluorescence microtomography ( $\mu$ XFCT) is a nondestructive analytical technique and has been widely used to nondestructively detect and quantify the elemental composition and distributions in samples. Usually, synchrotron radiation X-rays are used for  $\mu$ XFCT, due to its high flux density. In this paper, a laboratory-source-based  $\mu$ XFCT system was developed, in which a polycapillary lens is employed to focus the X-ray beam and improve the flux density. The maximum likelihood expectation maximization algorithm was used to reconstruct the computed tomography slices at a limited number of projections. The experimental results demonstrated that the developed system could reveal the elemental distribution inside the test sample, with an elemental sensitivity of 1000 ppm.

**Keywords** X-ray fluorescence microtomography · Polycapillary · Laboratory X-ray source

This work was supported by National Key R & D Program of China (Nos. 2017YFA0206004 and 2017YFA0403800) and the National Natural Science Foundation of China (Nos. 11775297 and U1532118).

✉ Biao Deng  
dengbiao@sinap.ac.cn

✉ Ti-Qiao Xiao  
xiaotiqiao@sinap.ac.cn

<sup>1</sup> Shanghai Institute of Applied Physics, Chinese Academy of Sciences, Shanghai 201800, China

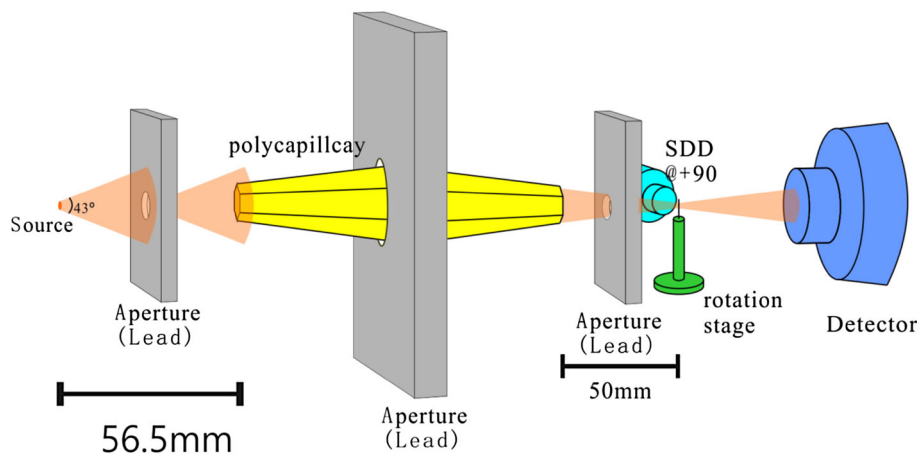
<sup>2</sup> University of Chinese Academy of Sciences, Beijing 100049, China

<sup>3</sup> Beijing Normal University, Beijing 100875, China

## 1 Introduction

As a unique methodology in the investigation of elemental distributions, X-ray fluorescence microtomography ( $\mu$ XFCT) based on synchrotron radiation has been applied to numerous fields since it was first proposed in 1986, including botany, biomedicine, medicine, material science, and mineralogy [1]. Numerous SR- $\mu$ XFCT systems have been established in synchrotron sources around the world, such as the European Synchrotron Radiation Facility (ESRF) in France [2], the Advanced Photon Source (APS) in America [3], Spring-8 in Japan [4], etc. To meet a user's requirements, a SR- $\mu$ XFCT system has been designed and constructed at the Shanghai Synchrotron Radiation facility (SSRF) [5–8]. However, the applications of SR- $\mu$ XFCT are limited by the complex and huge experimental facilities. In recent years, the laboratory  $\mu$ XFCT system underwent rapid development [9–12]. The laboratory  $\mu$ XFCT system has many merits, such as broader applications, availability, and convenience. The distribution of iron hydroxide was obtained with fluorescent computed tomography (CT) based on focused X-rays [13]. The gold nanoparticle distribution inside different organs of mice was measured with laboratory  $\mu$ XFCT [14]. Flux is the critical limitation of the laboratory  $\mu$ XFCT system. In this paper, a polycapillary lens [15–18], which is composed of many glass microcapillaries, is used to focus the X-rays from an X-ray tube and improve the flux density in CT scanning.

**Fig. 1** (Color online) Schematic layout of the laboratory  $\mu$ XFCT system



## 2 Set-up of the laboratory $\mu$ XFCT system

Figure 1 shows a schematic layout of the laboratory  $\mu$ XFCT system. The X-ray source is a micro-focus X-ray tube with a Tungsten target (Hamamatsu, 75 W). The energy of the X-ray beam is 70 keV. The opening angle of the X-ray beam is  $43^\circ$ . The distance between the polycapillary lens and the X-ray source is 56.5 mm. We added an aperture at the exit of the X-ray source to limit the divergence of the X-ray. In addition, the aperture behind the polycapillary lens was used to collimate the X-ray beam. The polycapillary lens is fixed on a 5D adjustable stage with a lead aperture. The focal distance of the polycapillary lens is 50 mm. The photons emitted by X-ray fluorescence were collected by a silicon drift detector (SDD) (SII, Vortex-90E) perpendicular to the incident X-ray beam in order to minimize X-ray scattering. The sample is mounted on a high-precision stage which can be adjusted in four dimensions. The X-ray CCD camera is used to detect the transmission images. For a better perspective of the imaging results, the transmission CT and  $\mu$ XFCT images can be fused together. A picture of the  $\mu$ XFCT system is shown in Fig. 2.

## 3 Polycapillary lens for $\mu$ XFCT

The opening angle of the laboratory X-ray source is quite large, which limits the flux density of the emitted X-ray beam. Low flux density is a key limitation for the development of a laboratory  $\mu$ XFCT system. Among all the X-ray focusing strategies, the use of a polycapillary lens is a cost-effective and highly efficient candidate [19, 20], which has large acceptance aperture and high transmission efficiency. Therefore, the use of a polycapillary lens to focus X-rays is feasible in a laboratory  $\mu$ XFCT system. For the CT imaging system, a pencil beam is usually used to achieve the projections. This means that, for the case of a

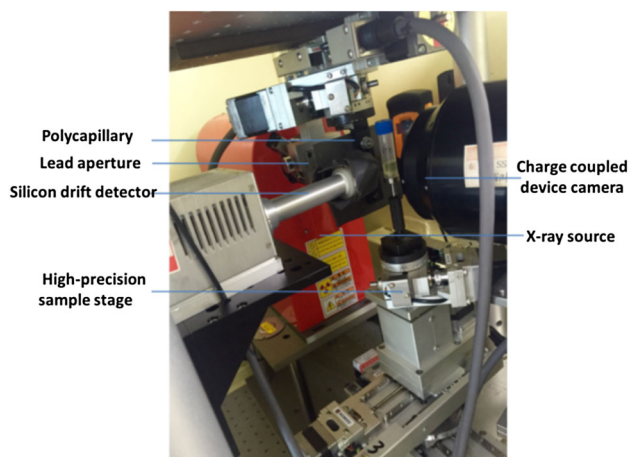


**Fig. 2** (Color online) Laboratory X-ray fluorescence microtomography system

focused beam, the depth of focus (DOF) of the polycapillary lens is a key parameter. If the DOF is less than the size of the sample, or the sample is not placed within the focal depth, the focused X-ray along the sample is divergent. This will result in an inaccurate reconstruction of the sample. Hence, the DOF of the polycapillary determines the maximum size of the experimental samples. The relationship between the DOF of the polycapillary lens and the sample size is shown in Fig. 3.

Before experiments, the depth of focus for the polycapillary lens was tested. As shown in Fig. 1, the polycapillary lens is fixed in the center of the aperture. The distribution of the focal spot is approximately Gaussian. The full width at half maximum (FWHM) of the Gaussian distribution at the capillary focal spot is defined as the focal spot size. We adjusted the rotation angle and the pitch angle of the polycapillary lens in order to obtain the best focus spot.

The focused spot was recorded by an X-ray CCD. The optimum position of the capillary was determined by

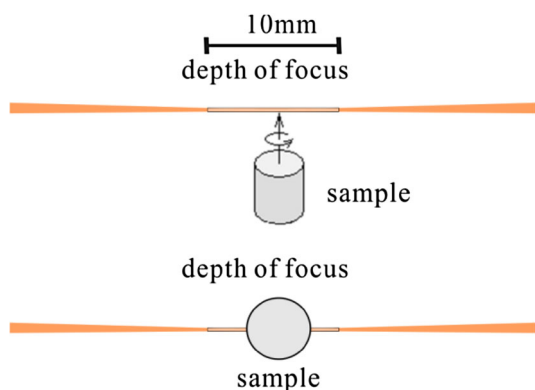


**Fig. 3** (Color online) Relationship between the focal depth of the polycapillary lens and sample size

measuring the intensity profile of the focused spot in the vertical and horizontal directions. When the distance between the polycapillary lens and the X-ray CCD was set to 50 mm, as shown in Fig. 4a, the size of each pixel was 13 μm and the FWHM of the polycapillary was 82 μm × 82 μm. To measure the focal depth, the X-ray CCD was scanned along the optical axis of the incident X-ray beam in 1 mm steps. According to the experimental results, the focal spot size remains 82 μm × 82 μm when the lens–detector distance ranged from 47 to 54 mm, as shown in Fig. 4c. This indicated that the DOF of the polycapillary lens was 7 mm. Therefore, the spatial resolution of the μXFCT system is 82 μm, and size of the sample should be less than 7 mm.

### 4 Image reconstruction algorithm for μXFCT

In a typical μXFCT system, the sample is scanned point-by-point with a pencil beam of synchrotron X-rays, which requires a significant data acquisition time to collect all the projections required for 3D tomographic imaging. Reducing the projection number is a practical solution to improve

the data collection efficiency. However, the limited projections always lead to fake images and increased noise during CT reconstruction. Seeking proper algorithm for image reconstruction is critical in the μXFCT system.

Among CT reconstruction algorithms, including FBP [12], algebraic reconstruction techniques (ART), ordered subset expectation maximization (OSEM), and maximum likelihood expectation maximization (MLEM), etc., the MLEM has a unique advantage for sparse projection data. Hence, the laboratory μXFCT system adopts the MLEM algorithm to reconstruct the projection data.

The principle of the MLEM algorithm is shown in the following equation [21, 22]:

$$C^{l+1}(i, j) = \frac{C^l(i, j)}{\sum_{(m, n)} K(i, j, m, n)} \sum_{(m, n)} \frac{K(i, j, m, n) I(m, n)}{\sum_{(i', j')} K(i', j', m, n) C^l(i', j')} \tag{1}$$

$C^l(i, j)$  and  $C^{l+1}(i, j)$  are the  $l$  and  $l + 1$  iterative image values, respectively, and  $I(m, n)$  is the fluorescence intensity for the  $n$ th projection under the  $m$ th projection angle.  $K(i, j, m, n)$  is the contribution of pixel  $(i, j)$  to the fluorescent intensity  $I(m, n)$ . In this case, the sample absorption of the incident and fluorescence X-rays is not taken into account. The distance from the center of each pixel  $(i, j)$  to the incident ray  $(m, n)$  is  $\Delta d$ , and  $d$  is the size of each pixel.

$$K(i, j, m, n) = \begin{cases} 1 & \Delta d \leq d/2 \\ 0 & \Delta d > d/2 \end{cases} \tag{2}$$

To test and verify the feasibility of the algorithm, numerical simulation was carried out on a phantom. The FBP, OSEM, and MLEM algorithms were used to reconstruct the CT images with different projection number. In the OSEM algorithm [23], the projection data were divided into several subsets according to the projection angles in order to improve the reconstruction speed. When the

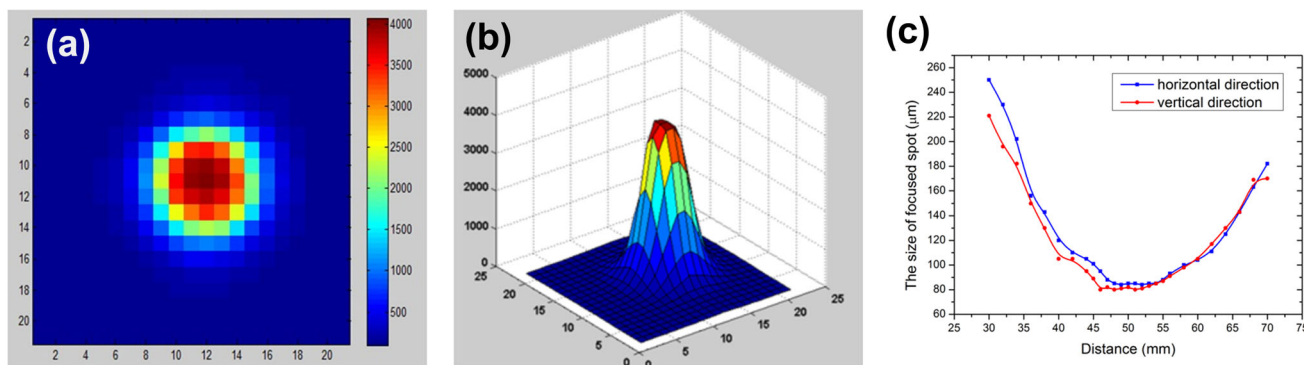


**Fig. 4** (Color online) **a** Intensity profile of the focal spot for the polycapillary lens. **b** Three-dimensional display of the focal spot. **c** Relationship between the focal spot size and the lens–detector distance in the horizontal and vertical direction

number of subsets is set to one, the OSEM algorithm and MLEM algorithm are the same.

Two phantoms, numbered in model 1 and model 2, were employed for the simulation. The bright patterns indicate the elemental distribution at a fixed concentration, and the size of each pixel is  $10\ \mu\text{m}$ . A total of 30, 20, and 10 projections were collected for the each model by rotating the model from  $0^\circ$  to  $180^\circ$  in steps of  $6^\circ$ ,  $9^\circ$ , and  $18^\circ$ , respectively. The reconstruction results of the models using the different algorithms are shown in Fig. 5. According to Fig. 5, even at the largest number of projections (30), the signal-to-noise ratio (SNR) of the reconstructed slices by MLEM algorithm is much higher than the FBP algorithm, in which obvious artifacts can be observed. When the projection number is reduced to 20, artifacts or noises arise in the reconstructed slices when using the MLEM algorithm. The slices reconstructed with the FBP algorithm become blurred, especially for model-I with a complex elemental distribution. When 10 projections were used in the reconstructed slices from MLEM, the complex elemental distribution of model-I can still be distinguished dimly, while the image reconstructed by FBP is indecipherable. Based on the simulation results shown in Fig. 5, we can conclude that MLEM is a much better algorithm than the FBP algorithm while dealing with fewer projections and at a limited projection number. MLEM is able to achieve acceptable image quality, even for a complex

elemental distribution. The results could be used as reasonable guidance in related experiments.

In the OSEM algorithm, adopting the subset is a useful way to increase the speed of convergence. However, when the number of subsets exceeds a critical value, the quality of the reconstructed images decreases with an increasing number of subsets. When the number of subsets exceeds the critical value, the noise will be amplified during the iterative CT reconstruction process with limited projections [24]. Considering the reconstruction efficiency, the MLEM algorithm only requires 0.635 s of computation time for 20 projections, and there is no need for acceleration. According to the concentration profiles, the MLEM algorithm can achieve a better signal-to-noise ratio (SNR) than the OSEM algorithm to some extent, as shown in Fig. 6.

Numerical simulation demonstrates the validity of the MLEM algorithm and highlights its reconstruction merits for sparse projection data. The simulation results show that the MLEM algorithm can effectively suppress noise, improve SNR, and reduce distortion in the reconstructed images. The MLEM algorithm can achieve acceptable image quality with a reduced projection number, resulting in higher data collection efficiency and lower radiation dose compared to FBP.

## 5 Experimental results and discussion

In the laboratory  $\mu\text{XFCT}$  system, the maximum voltage of the X-ray tube is 150 kV. The energy of the X-ray beam was estimated to be 70 keV. The focused beam size was  $82\ \mu\text{m} \times 82\ \mu\text{m}$ . A series of test samples were used to evaluate the capabilities of the  $\mu\text{XFCT}$  system. The first test sample was a thin walled borosilicate capillary with an outer diameter of 2 mm and a wall thickness of  $20\ \mu\text{m}$ . The capillary was filled with standard iodine solution. Iodine is a key element in biological research and plays an important role in clinical disease diagnosis. Iodine solution ( $1000\ \mu\text{g}/\text{ml}$ , 50 ml) is a standard reference material according to the National Institute of Standards and Technology (NIST, USA). As shown in Fig. 7a, the capillary was filled with 1000 ppm iodine solution. The sample was mounted on a high-precision stage and adjusted within the depth of focus. The sample was scanned with 40 translations per  $150\ \mu\text{m}$ . The exposure time per step was 6 s, and a  $6^\circ$  angular interval was used for CT scanning. The iodine distribution reconstructed by MLEM algorithm is shown in Fig. 7b. Figure 7c shows the acquired fluorescence spectrum (sinogram data). The ordinate is the scanning angle in degrees ( $0$ – $180^\circ$ ), and the abscissa is the number of translations. We can obtain the iodine distribution using the experiment system and achieve an elemental sensitivity of

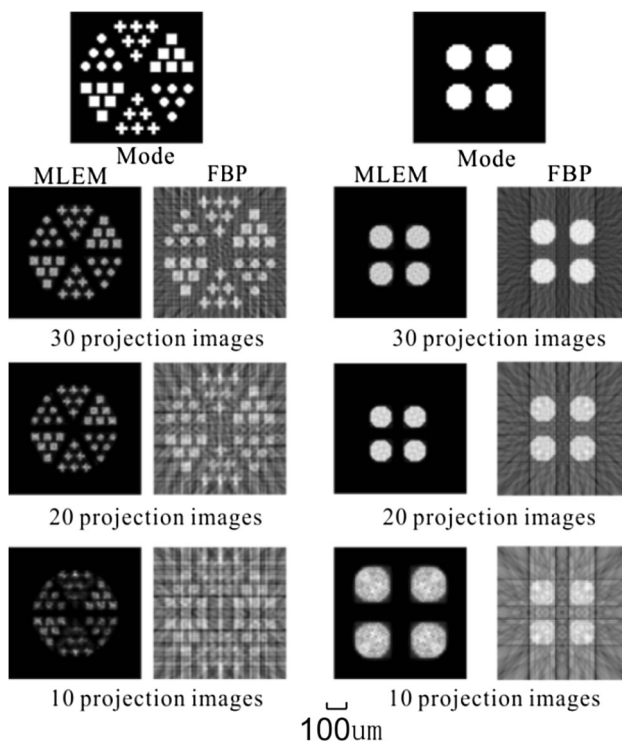


**Fig. 5** Comparison between the reconstructed slices by FBP and MLEM algorithms, respectively

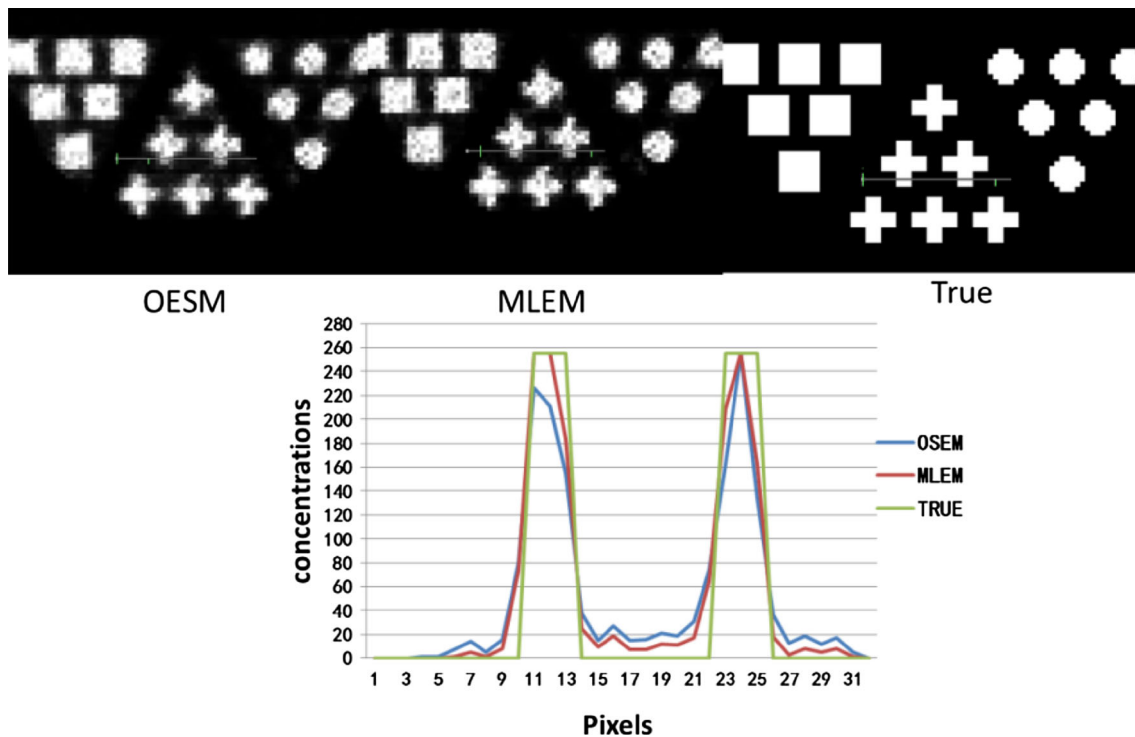


**Fig. 6** (Color online) Comparisons of the profiles between the OSEM and MLEM with various iterations

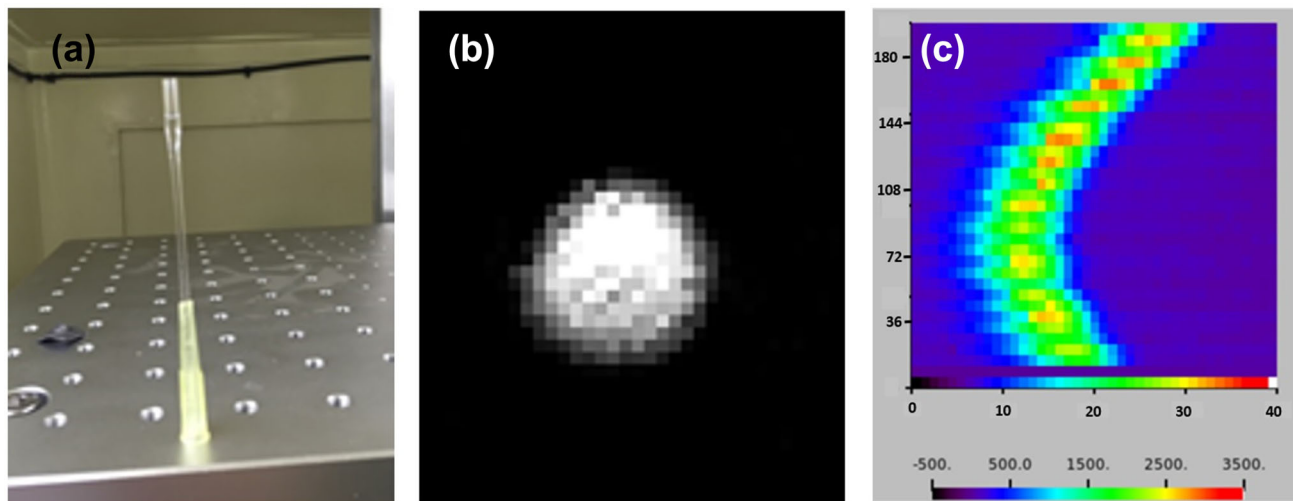


**Fig. 7** (Color online) Experimental results of the iodine, where **a** picture of the capillary filled with 1000 ppm iodine solution; **b** reconstructed iodine concentration; **c** the acquired fluorescence spectra

1000 ppm for iodine. The sensitivity depends on the atomic number and the flux on the sample.

For another test sample, three iron nails were selected, each with a diameter of 1 mm. The iron nails were placed in the depth of focus of the polycapillary lens with a triangular distribution. The phantom was scanned with 80 translation steps per 150  $\mu\text{m}$  at a  $6^\circ$  angular interval over  $180^\circ$ . The exposure time per step was 0.5 s. Figure 8b shows the reconstruction results for the nail sample. The

reconstruction results confirmed the actual distribution of the iron nails. Figure 8c shows two pieces of plastic pipe samples with a diameter of 1.5 mm, which were also chosen as test samples. The plastic pipes were filled with 10% iodine solution and bound tightly together with glue. The phantom was scanned with 60 translation steps per 150  $\mu\text{m}$  and a  $6^\circ$  angular interval over  $180^\circ$ . The exposure time per step was 2 s. As shown in Fig. 8d, the iodine distribution in different pipes can be distinguished. The shape of the iodine

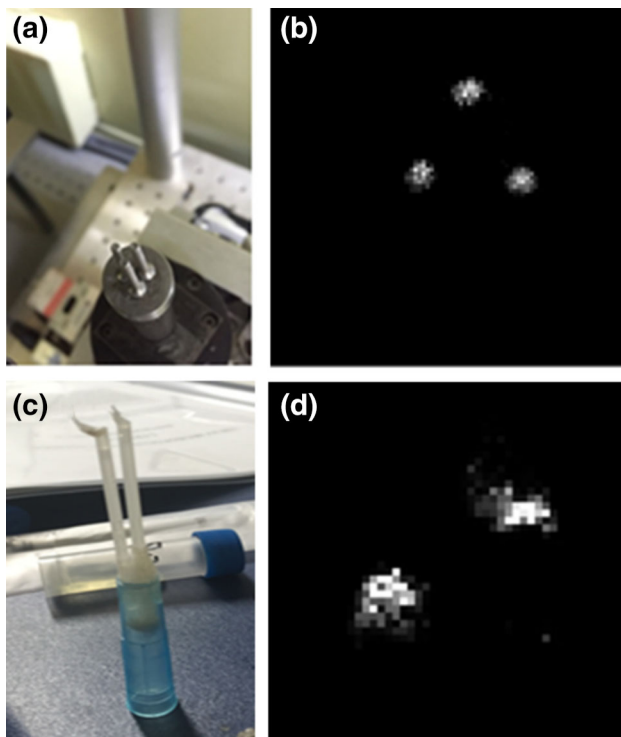


**Fig. 8** (Color online) Experimental results from iron nails and iodine. **a** Picture of three iron nails; **b** reconstruction slice for the three nails; **c** picture of two pieces of plastic pipes; **d** reconstruction slices of  $\mu$ XFCT for iodine concentration contained in the plastic pipes

distribution in the reconstructed slices is somewhat distorted due to solution overflow from the plastic pipe, which confirmed the spatial resolution of the laboratory  $\mu$ XFCT system.

## 6 Conclusion

A laboratory  $\mu$ XFCT system based on X-ray focusing by a polycapillary lens was successfully developed. The simulation and experimental results demonstrated the practicality of the system. The field of view for elemental imaging is 7 mm, and the elemental sensitivity is 1000 ppm. The developed system is to be opened to users, which will expand the applications of  $\mu$ XFCT in material science and biomedicine.

## References

1. R.P. Boisseau, *Determination of Three Dimensional Trace Element Distributions by the Use of Monochromatic X-ray Microbeams* (Massachusetts Institute of Technology, Department of Physics, Massachusetts, 1986)
2. A.S. Simionovici, B. Golosio, M.V. Chukalina, et al., Seven years of X-ray fluorescence computed microtomography, in *Optical Science and Technology, the SPIE 49th Annual Meeting, International Society for Optics and Photonics*, vol. 5535 (2004), pp. 232–242. <https://doi.org/10.1117/12.558948>
3. N.K. Blute, D.J. Brabander, H.F. Hemond et al., Arsenic sequestration by ferric iron plaque on cattail roots. *Environ. Sci. Technol.* **38**, 6074–6077 (2004). <https://doi.org/10.1021/es049448g>
4. Y. Hirai, A. Yoneyama, A. Hisada, et al., In vivo X-ray fluorescence microtomographic imaging of elements in single-celled fern spores, in *Synchrotron Radiation Instrumentation: Ninth International Conference on Synchrotron Radiation Instrumentation*, vol. 879(2007), pp. 1345–1348. <https://doi.org/10.1063/1.2436313>
5. B. Deng, G.H. Du, G.Z. Zhou et al., 3D elemental sensitive imaging by full-field XFCT. *The Analyst* **140**, 3521–3525 (2015). <https://doi.org/10.1039/C4AN02401J>
6. J. Qiu, B. Deng, Q. Yang et al., Internal elemental imaging by scanning X-ray fluorescence microtomography at the hard X-ray microprobe beamline of the SSRF: preliminary experimental results. *Nucl. Instrum. Methods Phys. Res. Sect. B* **269**, 2662–2666 (2011). <https://doi.org/10.1016/j.nimb.2011.08.005>
7. B. Deng, Q. Yang, G.H. Du et al., The progress of X-ray fluorescence computed tomography at SSRF. *Nucl. Instrum. Methods Phys. Res. Sect. B* **305**, 5–8 (2013). <https://doi.org/10.1016/j.nimb.2013.04.045>
8. P.F. Sun, B. Deng, G.H. Du et al., Nondestructive rare earth element imaging of fish teeth from deep-sea sediments. *X-ray Spectrom.* **44**, 442–446 (2015). <https://doi.org/10.1002/xrs.2624>
9. P.F. Sun, B. Deng, Q. Yang et al., An accelerated OSEM reconstruction algorithm using an accelerating factor for X-ray fluorescence tomography. *Nucl. Tech.* **38**, 060201 (2015). <https://doi.org/10.11889/j.0253-3219.2015.hjs.38.060201>. (in Chinese)
10. H.L. Xie, B. Deng, G.H. Du et al., Latest advances of X-ray imaging and biomedical applications beamline at SSRF. *Nucl. Sci. Tech.* **26**, 020102 (2015). <https://doi.org/10.13538/j.1001-8042/nst.26.020102>
11. H. von Busch, G. Harding, G. Martens et al., Investigation of externally activated X-ray fluorescence tomography for use in medical diagnostics. *Med. Imaging Int. Soc. Opt. Photonics* **5745**, 90–101 (2005). <https://doi.org/10.1117/12.591663>
12. N. Manohar, B.L. Jones, S.H. Cho, Improving X-ray fluorescence signal for benchtop polychromatic cone-beam X-ray fluorescence computed tomography by incident X-ray spectrum optimization: a Monte Carlo study. *Med. Phys.* **41**, 101906 (2014). <https://doi.org/10.1118/1.4895004>
13. S.-K. Cheong, B.L. Jones, A.K. Siddiqi et al., X-ray fluorescence computed tomography (XFCT) imaging of gold nanoparticle-loaded objects using 110 kVp X-rays. *Phys. Med. Biol.* **55**, 647 (2010). <https://doi.org/10.1088/0031-9155/55/3/007>
14. H.M. Hertz, J.C. Larsson, U. Lundstrom et al., Laboratory X-ray fluorescence tomography for high-resolution nanoparticle bio-imaging. *Opt. Lett.* **39**, 2790–2793 (2014). <https://doi.org/10.1364/ol.39.002790>
15. M.A. Kumakhov, Channeling of photons and new X-ray optics. *Nucl. Instrum. Methods Phys. Res. Sect. B* **48**, 283–286 (1990). [https://doi.org/10.1016/0168-583X\(90\)90123-C](https://doi.org/10.1016/0168-583X(90)90123-C)
16. M.A. Kumakhov, F.F. Komarov, Multiple reflection from surface X-ray optics. *Phys. Rep.* **191**, 289–350 (1990). [https://doi.org/10.1016/0370-1573\(90\)90135-O](https://doi.org/10.1016/0370-1573(90)90135-O)
17. P. Korecki, K.M. Sowa, B.R. Jany et al., Defect-assisted hard X-ray microscopy with capillary optics. *Phys. Rev. Lett.* **116**, 233902 (2016). <https://doi.org/10.1103/PhysRevLett.116.233902>
18. K.M. Sowa, A. Last, P. Korecki, Grid-enhanced X-ray coded aperture microscopy with polycapillary optics. *Sci. Rep.* **7**, 44944 (2017). <https://doi.org/10.1038/srep44944>

19. B. Laforce, B. Vermeulen, J. Garrevoet et al., Laboratory scale X-ray fluorescence tomography: instrument characterization and application in earth and environmental science. *Anal. Chem.* **88**, 3386–3391 (2016). <https://doi.org/10.1021/acs.analchem.6b00137>
20. N. Manohar, F.J. Reynoso, P. Diagaradjane et al., Quantitative imaging of gold nanoparticle distribution in a tumor-bearing mouse using benchtop X-ray fluorescence computed tomography. *Sci Rep.* **6**, 22079 (2016). <https://doi.org/10.1038/srep22079>
21. L.A. Shepp, Y. Vardi, Maximum likelihood reconstruction for emission tomography. *IEEE Trans. Med. Imaging* **1**, 113–122 (1982). <https://doi.org/10.1109/TMI.1982.4307558>
22. P.J. Green, Bayesian reconstructions from emission tomography data using a modified EM algorithm. *IEEE Trans. Med. Imaging* **9**, 84–93 (1990). <https://doi.org/10.1109/42.52985>
23. Q. Yang, B. Deng, W. Lv et al., Fast and accurate X-ray fluorescence computed tomography imaging with the ordered-subsets expectation maximization algorithm. *J. Synchrotron Radiat.* **19**, 210–215 (2012). <https://doi.org/10.1107/S0909049511052253>
24. H.M. Hudson, R.S. Larkin, Accelerated image-reconstruction using ordered subsets of projection data. *IEEE Trans. Med. Imaging* **13**, 601–609 (1994). <https://doi.org/10.1109/42.363108>